Food Chemistry: X 24 (2024) 101856

Contents lists available at ScienceDirect

Food Chemistry: X

journal homepage: www.sciencedirect.com/journal/food-chemistry-x

Ponceau 4R elimination from fruit juice: An integrated optimization strategy utilizing artificial neural networks, least squares, and chitosan-nickel ferrite Nano Sorbent

Samira Shokri [a], Nabi Shariatifar [a,*], Ebrahim Molaee-Aghaee [a,*], Gholamreza Jahed Khaniki [a], Parisa Sadighara [a], Somaye Vali Zade [b], Shahram Shoeibi [c]

[a] Department of Environmental Health, Food Safety Division, School of Public Health, Tehran University of Medical Sciences, Tehran, Iran
[b] Halal Research Center of IRI, Food and Drug Administration, Ministry of Health and Medical Education, Tehran, Iran
[c] Food and Drug Laboratory Research Center, Food and Drug Administration, Iran Ministrily of Health and Medical Education, Iran

ARTICLE INFO

Keywords:
Chitosan
Fruit juice
Response surface methodology
Nickel ferrite
Ponceau 4R
Artificial neural network
Radial basis function

ABSTRACT

The goal of present work is to examine the efficiency of aminated-chitosan/$NiFe_2O_4$ nanoparticles (AmCs/$NiFe_2O_4$ NPs) produced for removing Ponceau 4R (P4R) from fruit juice through an adsorption process. The resulting nanoparticles were characterized using various techniques. The modeling of results was done using least squares (LS) and *Radial basis function*-artificial neural network (RBF-ANN). The optimum removal of P4R (91.43 %) was obtained at the following optimum conditions: pH 4.47, adsorbent dosage 0.047 g/L, contact time approximately 57.78 min, and initial concentration P4R 26.89 mg/L. The highest adsorption capacity (qm) was found to be 208.33 mg g^{-1}. The P4R adsorption mostly followed the Freundlich and pseudo-second-order isotherm kinetic models. Both LS-based models and RBF-ANN provided good predictions for independent variables. The dye elimination efficacy for juice samples were approximately 90.34 %. Therefore, based on the obtained results, it can be claimed that the prepared AmCs/$NiFe_2O_4$ NPs can be used to remove P4R.

1. Introduction

Juice adulteration is a significant economic issue, regulatory agencies are currently facing major adulteration issues, involving sophisticated manipulations such pulp wash, juice admixture, organic acids, amino acids, and the addition of dyes (Dehelean, 2013, Wan et al., 2018). Dyes are widely utilized in various industries, including drug, cosmetic, and food, for producing various products such as sweets, gums, juices, puddings, mustard, and drugs (Piccin et al., 2009).

The amount and type of food colors allowed in different countries are different (Choi, 2012, Rouhani & Pirkarimi, 2018, Yoshioka & Ichihashi, 2008). In Iran, synthetic dyes including quinoline yellow, sunset yellow, brilliant blue, indigotin, Ponceau 4R, azorbin and allurard are allowed for use in food production (Anonymous). In addition the use of permitted food dyes Ponceau 4R in certain products, including ice creams, beverages, juices, desserts, and traditional ones, has been banned (Anonymous, Anonymous). Ponceau 4R has been banned in many countries based on the approvals of the Joint FAO/WHO Committee on Food Additives due to its harmful effects (Helal et al., 2006; Tsuda et al., 2001).

Various analytical techniques have been reported to separate, identify, and measure food colorants. The common approaches include physical and observational procedures, chromatography, spectroscopy, PCR, and those based on sensors like *E*-nose and E-tongue (Hong et al., 2017; Stozhko et al., 2022). The main disadvantages of most of these techniques are time-consuming and complex sample preparation and analysis, expensiveness, and the need for an expert operator. Therefore, developing fast, sensitive, cheap, and simple methods is crucial in detecting adulteration in food samples (Oliveri & Downey, 2012).

The development of effective adsorbents with excellent removal capabilities for the adsorption of dye in food items remains extremely challenging. In this regard, for dyes elimination from aqueous solutions, several researches are being conducted to synthesize non-toxic, strong, high-performance adsorbents (Masood et al., 2020).

Chitosan is a cheap and plentiful biopolymer that has been utilized as a bio-sorbent to remove dye from aqueous solutions because of its good biodegradable, biocompatible, polymeric nature, and non-toxic qualities (Homayonfard et al., 2020). Chitosan's unique poly cationic

* Corresponding authors.
E-mail addresses: nshariatifar@alumni.ut.ac.ir (N. Shariatifar), emolaeeaghaee@sina.tums.ac.ir (E. Molaee-Aghaee).

https://doi.org/10.1016/j.fochx.2024.101856
Received 20 July 2024; Received in revised form 20 September 2024; Accepted 24 September 2024
Available online 25 September 2024

structure allows for ion exchange with anions, owing to its protonation of amine groups in acidic media. Its chelating properties are related to its high functional groups (Ackah et al., 2014).

After the adsorption process, chitosan-based adsorbents might be difficult to sequester from the aqueous solution using traditional separation techniques like filtration and sedimentation because they can clog the filters or disappear. Additionally, because adsorbent materials produce sludge when released into the environment, they might lead to secondary contamination (Kefeni et al., 2017; Reddy & Lee, 2013). Recently, magnetic separation ($NiFe_2O_4$) has been widely used as an efficient process for the separation and recycling of adsorbent materials. This technology's primary benefit is its ability to quickly separate, while consuming the least amount of energy and creating no contaminants (Kefeni et al., 2017, Reddy & Lee, 2013).

RSM is a statistical technique used to estimate the impact of input variables on output responses, defining the role of independent variables or combinations (Pervukhin et al., 2023). In addition, ANN modeling is a new approach that has recently attracted the attention of researchers. This technique is capable of estimating the nonlinear relationship between independent variables and solves problems that cannot be solved by traditional statistical methods (Giordano et al., 2017). One of the limiting factors of using RSM technique is that it does not include incontrollable variables. While neural network modeling is not affected by physical or chemical process. Therefore, by using ANN, a stable nonlinear simulation model can be created. Additionally, the drawbacks of RSM can be addressed by employing RBF-ANN modeling, which allows experimental data to be used to study the true link between independent parameters and response (Carabajal et al., 2020; Teglia et al., 2020).

The purpose of this study was to optimize P4R dye removal on AmCs/$NiFe_2O_4$ NPs using LS and RBF-ANN modeling for response prediction. The RSM methodology was utilized to determine the optimal conditions of the procedure variables, including the effects of pH, contact time, and initial dose on AmCs/$NiFe_2O_4$ NPs' sorption capacity and dye adsorption. Furthermore, examination of adsorption actions was performed kinetic models, and Freundlich and Langmuir isotherms.

2. Experimental sections

2.1. Materials

Chitosan was supplied by Merck Company (Darmstadt, Germany). The chemicals NaOH, $NiCl_2{\bullet}6H_2O$, $FeCl_3{\bullet}6H_2O$, oleic acid, acetic acid (>98 %), ethylenediamine (EDA; 99 %), calcium chloride ($CaCl_2$), and 1-ethyl-3-(3-dimethylaminopropyl) carbodiimide (EDC) were also provided by Merck Company (Darmstadt, Germany).

2.2. Synthesis of $NiFe_2O_4$ NP_S

First, aqueous solutions of $NiCl_2{\bullet}6H_2O$ (0.5 g/10 mL deionized water), and $FeCl_3{\bullet}6H_2O$ (1.5 g/50 mL deionized water) are mixed together and stirred for 30 min at 60 °C until a homogenous solution was obtained. Droplets of 0.2 M NaOH were then added to the pH solution to bring it to 11. The mixture was then agitated for roughly 40 min at 80 °C.

After obtaining the desired dark brown precipitates, they underwent filtration, a deionized water wash, and room temperature drying. Then, they were placed in a furnace with 600 °C for 3 h (Ahmad et al., 2023; Rezagholizade-shirvan et al., 2022; Rezagholizade-shirvan et al., 2023; Shokri et al., 2023).

2.3. Synthesis of of aminated chitosan (AmCs)

For 10 h at room temperature, 0.5 g of chitosan was treated in 300 mL of aqueous 0.5 M chloroacetic acid (pH = 8.0, adjusted with 0.1 M NaOH). To remove unreacted material, the mixture was then repeatedly washed. Then, the sample was submerged in 100 mL of 1.0 M ethylenediamine. The ethylenediamine solution was supplemented with 10 ml of EDC (1-ethyl-3,3-dimethylaminopropyl) carbodiimide (5 mM) for every 40 mg of specimen. After centrifugation, the aminated chitosan was collected and continuously rinsed with deionized water until the pH was around 7. Finally, it was dried for 24 h at 80 °C in an oven (Yousefi et al., 2024).

2.4. Synthesis of AmCs/$NiFe_2O_4$ NPs

0.25 g of $NiFe_2O_4$ NPs were added to a 50 mL solution of amine-modified chitosan. The solution was maintained at 50 °C for approximately 3 h, and then it was sonicated for about 30 min. Brown precipitates were collected, filtered, cleaned, dried at 60 °C for 12 h (Ahmad et al., 2023; Shokri et al., 2023; Shokri et al., 2024).

2.5. Characterization

Several physiochemical characterization methods were applied to the of AmCs/$NiFe_2O_4$ NPs that were produced. The structure of produced samples was analyzed with Fourier transform infrared spectroscopy (FTIR). This analyze was carried out 400–4000 cm^{-1} in range, with a 4 cm^{-1} resolution.

Using it, the validity of every functional group has been established. The "Bruker D-8 Advanced" instrument was utilized to obtain the X-Ray diffraction (XRD) spectrum, which was then analyzed to assess the material's crystallinity, particle size, and surface examination of the produced nanoparticles. For the morphological analysis, a Philips Co. scanning electron microscopy (SEM) (Czech, SEM, and MIRA3-LUM) & Transmission electron microscope (TEM) (Philips EM 208S, TEM, EM) were used.

2.6. Adsorption study

The LS based RSM method was utilized in Design Expert version 8.0.7.1 software to design sorption experiments and considering optimum values for all factor. A total 30 experiments were conducted with four factor two levels, and Data analysis was performed for the effectiveness of removal considering P value <0.05 as statistically significant. The produced solutions were centrifuged (4000 rpm, 10 min) for determination of sorption efficiency of AmCs/$NiFe_2O_4$ NPs. Then, absorbance of the solution was specified through measurement of the absorption at 505 nm. The dyes reduction (%), and adsorption value was evaluated by Eq. (A.1) and Eq. (A.2) respectively.

Where, C_i and C_e are the primary and final concentration of dye P4R (mg/L), respectively. V is the volume of sample (mL) and M is the mass of the sorbent (g) (Ghorbani et al., 2021; Gordi et al., 2020; Rose et al., 2023).

$$R\% = \frac{(C_0 - C_e)}{C_0} \tag{A.1}$$

$$q_e = \frac{V}{M}(C_0 - C_e) \tag{A.2}$$

2.7. Data modeling by ANN

Nonparametric techniques, like RBF-ANN, can reduce the issue of underfitting by employing three layers of neurons or nodes for optimization. Three layers make up RBFs, and these layers are the basic computing units. The input variables are dispersed into a single hidden layer via an input layer. A simple Gaussian function serves as the transfer function for each neuron in the buried layer. With one unit for each response, the output layer is linearly activated (Giordano et al., 2017). The network was trained to generate plots of predicted response values versus nominal values, prediction residuals versus nominal response values, and normal probability plots for residuals. Ultimately, the

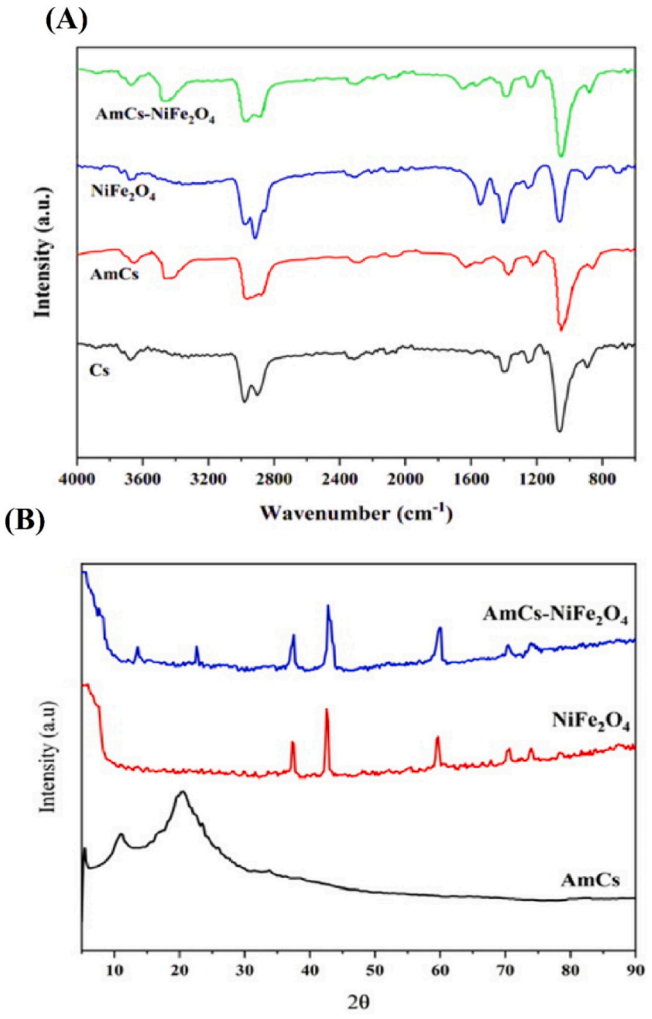

Fig. 1. The FTIR spectra and the XRD patterns of Cs, AmCs, $NiFe_2O_4$ NPs, AmCs/$NiFe_2O_4$ NPs.

network was optimized to effectively represent the data. The SRO_ANN MatLab toolbox was used for the implementation of the ANN.

2.8. Adsorption isotherms

The investigation of adsorbent behavior, and the dye's interaction, adsorption isotherms were carried out in environmental conditions with pH (4.47), 60 min, and different concentrations (10, 15, 20, 25, 30, 35, 40, 45, and 50 mg/L) of dyes. Adjustments of absorption data was done using Langmuir and Freundlich models.

2.9. Adsorption kinetics

Adsorption kinetic models (pseudo-first-order, and pseudo-second-order and Intraparticle diffusion) were applied to control and evaluate the process of P4R adsorption by synthesized AmCs/$NiFe_2O_4$ NPs. Kinetic investigations were carried out under different contact times (from 10 to 80 min) and, 10 mL of spiked P4R solution by a concentration of 26.89 (mg/L^{-1}), optimum sorbent dose (0.047 g), and pH = 4.47 (Solano et al., 2021).

2.10. Real sample study

In order to investigate the effect of sample matrix on the removal of P4R dye, samples of Natural pomegranate juice were used. The fruit juice samples were filtered, and then spiked with 20 ppm P4R. Synthetic nanoparticles were added to the sample solutions at a ratio of 0.47 g and remained at 20 °C for approximately 57.78 h. After the allotted time, the nanoparticles were extracted from the solution using a magnet. The absorbance of the samples was measured with a spectrophotometer at a wavelength of 505 nm, both before and after the addition of nanoparticles to the sample solution.

3. Results and discussion

3.1. FTIR analysis

FT-IR analyses were conducted on nanocomposites like Cs, AmCs, $NiFe_2O_4$, and AmCs/$NiFe_2O_4$, focusing on structural characteristics of samples. The specific FTIR spectra corresponding to Cs are shown in Fig. 1(A). Our research identified unique spectral characteristics associated with different functional groups in the chitosan polymer. The Cs structure was observed to contain amine groups and hydrocarbon chains, with N—H and O—H stretching band at range 3104 cm^{-1}–3679 cm^{-1} (Çınar et al., 2017; Mustafa, 2019). In the infrared spectrum, two absorption peaks are observed at 2922 cm^{-1} and 2869 cm^{-1}, which correspond to the symmetric and antisymmetric stretching vibrations of -CH_2. Another absorption peak is visible at 1603 cm^{-1}, attributed to the bending vibration of the amine group in chitosan. Additional peaks at 1403, 1251, and 1059 cm^{-1} are associated with C═O, N—H bending (amide), aromatic rings, C-O-H, and C—O stretching (Tsai et al., 2014; Yuvaraja et al., 2020). The broad bands observed in the FTIR spectrum of AmCs are attributed to the stretching vibrations of C—N and O—H, at 1062 and 3441 cm^{-1}, respectively. The AmCs/$NiFe_2O_4$ nanocomposite exhibited a shift of these bands to 3446 and 3452 cm^{-1}. Following the formation of C═N and primary amine groups in the prepared nanoparticles, it was observed that the characteristic vibration peaks of C═N and N—H at 1630 and 1540 cm^{-1} increased. Furthermore, the stretching vibration of the amide-I (C═O of NH-C═O) groups and the N—H bending of amide-II were attributed to the bands at 1645–1649 cm^{-1} and 1560 cm^{-1}, respectively. The broad band at 3441 cm^{-1} in the AmCs spectra, which corresponds to the stretching vibrations of -NH_2 groups, is among the observed characteristics. Additionally, the emergence of a distinctive peak at 1516 cm-1 indicates an increase in amide groups (-NHCO). The amine (N—H stretching vibration) and amide groups were responsible for the appearance of two new peaks at 1154 cm^{-1} and 1513 cm^{-1}, respectively. Each of these bands denotes the successful formation of long-range NH_2 groups on the surface of the nanoparticles.

The strong band at 694 cm^{-1} in the FTIR spectrum of $NiFe_2O_4$ is associated with the tetrahedral Fe—O stretching vibration bond and is the characteristic band of $NiFe_2O_4$. Sulphate ions adsorbed on the particle surface of $NiFe_2O_4$ are responsible for the sharp band at 1058 cm^{-1}. Additionally, the band at 1543 cm^{-1} is associated with N—H bending vibration. Peaks seen at 2977 and 2916 cm^{-1} are linked to aliphatic hydrogen vibration (–CH_2 stretching). Lastly, the stretching vibration mode of O—H groups is represented by the bands at 3357 cm^{-1} and 3678 cm^{-1} (Tsai et al., 2014; Yuvaraja et al., 2020). Furthermore, our examination identified distinct peaks at 757 and 823 cm^{-1}, respectively, which are associated with the bending vibrations of the Fe—O bonds (Ahmad et al., 2015; Mustafa, 2019). The results confirm that Cs was able to successfully coat $NiFe_2O_4$ nanoparticles. This was likely achieved through a chemical reaction and electrostatic contact between the negatively charged surface of nickel ferrite and the positively charged surface of chitosan.

3.2. XRD analysis

The XRD pattern for the AmCs/$NiFe_2O_4$ nanocomposite is displayed in Fig. 1 **(B).** Two weak peaks that appear in this pattern at 11.6° and 20.16° show that AmCS is semicrystalline. The main peaks in the $NiFe_2O_4$ NPs XRD pattern, with 2θ values of, 37.20°, 42.36°, 59.35°, and

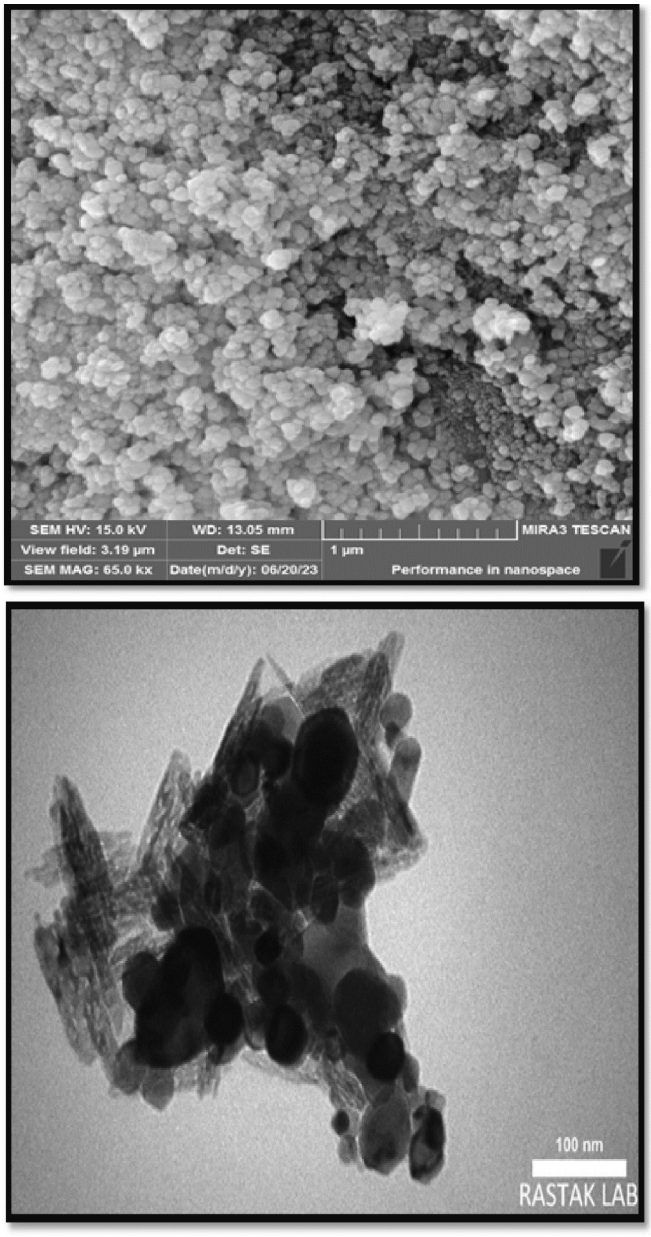

Fig. 2. The SEM and TEM images of AmCs/$NiFe_2O_4$ NPs.

71.58° correspond to the crystal planes (311), (400), (440), and (533) respectively. These peaks confirm that the nickel ferrite nanoparticles have fully crystallized. Major diffraction peaks related to the bonding of $NiFe_2O_4$ nanoparticles to AmCs were observed at 2θ values of 11.6°, 20.16°, 37.20°, 59.85°, 71.58°, and 75.49° in the XRD pattern of AmCs/$NiFe_2O_4$. Therefore, the successful and impurity-free synthesis of the AmCs/$NiFe_2O_4$ nanocomposite is confirmed (Yuvaraja et al., 2020).

3.3. SEM analysis

The morphology AmCs/$NiFe_2O_4$ NPs (Fig. 2 **(A))** was examined using SEM techniques. An elevation in kinetic energy results in particle destabilization, leading to a heightened propensity for aggregation and subsequent enlargement of the particle size. Chitosan adsorbed on particles reduces surface tension, forming spheres with appropriate surface-to-volume ratio, resulting in well-differentiated nanospheres with floatability after initial precipitation. SEM micrographs show successful incorporation of $NiFe_2O_4$ into the chitosan matrix, that chitosan effectively prevents particle adhesion and confirms its coating. These findings are consistent with previous studies (Ansari et al., 2022; Ramezani et al., 2016).

3.4. TEM analysis

The TEM was used to assess the micromorphology of AmCs/$NiFe_2O_4$ NPs, and the results are shown in **(**Fig. 2 **(B)).** The AmCs/$NiFe_2O_4$ NPs exhibit uniformity, spherical shape, and near monodispersity. They display a deeper-colored particle core in the chitosan-coated magnetic nanoparticles. As $NiFe_2O_4$ NPs are distributed throughout the chitosan solution during the sorbent's synthesis, there is also a decrease in their tendency to aggregate. The picture shows that the sorbent's structure is irregular, with chitosan NPs typically creating rod-shaped particles and being placed on some regions of the $NiFe_2O_4$ NPs' surface.

3.5. LS Modeling of Response Surface

The study focuses on optimizing process variables like pH, concentration dye, contact time, and sorbent dosage using a central composite design (CCD) and analyzing their interaction with dye extraction. The parameters are presented in Table 1, focusing on optimization using the conventional method and multiple linear regression based RSM.

3.6. Analysis of variance (ANOVA)

A mathematical model is constructed for each response by fitting a polynomial function of the second order or higher, and the significance of the coefficients is examined using an ANOVA test. When the regression is significant at the selected confidence level and the lack of fit (LOF) is not statistically significant, the model is considered to be good. The Model F-value of 31.74 suggests that the model is statistically significant. There is a mere 0.01 % probability that such a large F-value could arise due to random variation. *P*-values below 0.0500 indicate that model terms are statistically significant. The suggested model successfully captures the experimental results, as indicated by the *p*-value for lack of fit (LOF). In this scenario, A, B, C, D, AB, BC, CD, C^2, and D^2 were considered significant model terms **(**Table 1**).**

In the model, the estimated R^2 shows how effectively the model predicts responses from unknown data; for good models, it should be close to 1 For the model, it is desired and observed that R^2 (0.96), adjusted R^2 (0.9369), and Predicted R^2 (0.8661) are near each other (the difference is less than 0.2). Adeq precision calculates the ratio of signal to noise. A ratio (20.01) greater than 4 is desirable. The study shows a coefficient of variance (CV) of 3.65.

Table 1 displays the coefficients of variables and their impact on the response. The result reveals that time of adsorption, sorbent amount, and pH are significant factors for dye adsorption, with the pH having the highest effect on the experimental response. Fig. 3 presents a systematic investigation of the effects of various parameters on P4R removal, with each subplot focusing on the impact of a single variable while holding others constant at their respective center points. This approach allows for a clear understanding of individual parameter contributions, but it's important to note that the analysis does not account for potential interactions between these factors. Fig. 3A: The influence of P4R concentration on removal efficiency demonstrates a non-linear relationship. Initially, a slight increase in removal percentage is observed with increasing P4R concentration up to 30 mg/L. However, further increases in concentration lead to a slight decrease in removal efficiency. This trend suggests that the adsorption process may be influenced by factors such as site saturation at higher P4R concentrations. Fig. 3B: The amount of adsorbent significantly affects P4R removal. As the adsorbent dosage increases from 0 to 0.04 g, the removal percentage of P4R increases. Beyond this point, the removal percentage plateaus, indicating that the available adsorption sites are approaching saturation. This observation supports the hypothesis that an increased adsorbent dosage

Table 1
The ANOVA test for P4R adsorption on AmCs/$NiFe_2O_4$ NPs.

Factor	Name	Units	Minimum	Maximum	Mean ± S.d
A	Color Concentration	mg/L	10.00	50.00	30.00 ± 15.76
B	Sorbent amount	g/L	0.0200	0.0600	0.0400 ± 0.0158
C	Adsorption time	min	20.00	70.00	45.00 ± 19.70
D	pH	–	3.00	9.00	6.00 ± 2.36

Source	Sum of Squares	df	Mean Square	F-value	p-value	
Model	3686.69	14	263.33	31.74	< 0.0001	**significant**
F_1-Color Concentration	88.62	1	88.62	10.68	0.0052	
F_2-Sorbent amount	102.05	1	102.05	12.30	0.0032	
F_3-Adsorption time	647.52	1	647.52	78.06	< 0.0001	
F_4-pH	1432.73	1	1432.73	172.71	< 0.0001	
F_1F_2	41.99	1	41.99	5.06	0.0399	
F_1F_3	19.85	1	19.85	2.39	0.1428	
F_1F_4	3.76	1	3.76	0.4537	0.5108	
F_2F_3	83.91	1	83.91	10.11	0.0062	
F_2F_2	15.64	1	15.64	1.89	0.1899	
F_3F_4	267.00	1	267.00	32.19	< 0.0001	
F_1^2	31.63	1	31.63	3.81	0.0698	
F_2^2	0.6326	1	0.6326	0.0763	0.7862	
F_3^2	52.10	1	52.10	6.28	0.0242	
F_4^2	52.91	1	52.91	6.38	0.0233	
Residual	124.43	15	8.30			
Lack of Fit	100.98	10	10.10	2.15	0.2056	**not significant**
Pure Error	23.45	5	4.69			
Cor Total	3811.12	29				

provides more binding sites, thereby enhancing P4R removal. Fig. 3C: The removal time emerges as a crucial factor influencing P4R removal. The removal percentage significantly increases with increasing contact time up to 45 min, highlighting the importance of sufficient residence time for effective adsorption. Beyond this point, the removal percentage plateaus, indicating a near-equilibrium state where the adsorption process has reached its maximum capacity within this timeframe. Fig. 3D: pH plays a significant role in P4R removal. The removal percentage decreases significantly with increasing pH values. This phenomenon can be attributed to changes in the surface polarity of both the adsorbent and P4R, leading to reduced electrostatic interactions between the two. This alteration in surface properties reduces the affinity of the adsorbent for P4R, consequently hindering the removal process.

The interaction between P4R concentration and sorbent amount (F_1*F_2), sorbent amount and contact time (F_2*F_3), sorbent amount and pH (F_2*F_4), and pH and contact time (F_3*F_4), also significantly affects the response. Fig. 4 delves into the effects of significant interactions on P4R removal, showcasing the interplay of different factors and their impact on overall removal efficiency. Fig. 4A demonstrates a synergistic effect between P4R concentration and adsorbent dosage. As both factors increase simultaneously, the removal percentage of P4R also increases. This positive correlation suggests that higher P4R concentrations can be effectively removed by increasing the amount of adsorbent, indicating a direct and proportional relationship between these parameters. A similar trend is observed in Fig. 4B, highlighting the combined impact of removal time and adsorbent dosage. The removal percentage increases with increasing removal time, suggesting that longer contact times allow for more effective adsorption. However, the effect of changes in removal time appears to have a greater influence on the P4R removal than the amount of adsorbent. This implies that the adsorption process is particularly sensitive to the contact time, emphasizing its critical role in achieving higher removal efficiencies (Sadegh et al., 2022).

Fig. 4C showcases the combined effects of pH and adsorbent dosage on P4R removal. A decrease in pH alongside an increase in adsorbent dosage leads to a significant improvement in the P4R removal. This observation highlights the importance of acidic conditions for effective P4R removal using the investigated adsorbent. The increased removal efficiency in acidic environments can be attributed to enhanced electrostatic interactions between the adsorbent and the P4R molecules due to favorable pH-dependent surface charges. Fig. 4D illustrates the combined effect of removal time and pH on the P4R removal. The removal percentage increases with increasing removal time and decreasing pH. This suggests that longer contact times and acidic conditions promote the P4R removal, highlighting the direct and inverse relationship between time and pH, respectively, on the removal process (Roosta et al., 2015).

The percentage decolorization was calculated using a quadratic polynomial semi-empirical expression, as demonstrated in Eq. (A.3).

$$\begin{aligned}\text{Removal Efficiency} =& 74.45249 + 0.52302^{*}\,F_1 + -208.595^{*}\,F_2 \\ &+ 0.44245^{*}\,F_3 + -0.301058^{*}\,F_4 + 4.05^{*}\,F_1F_2 + \\ &- 0.0022275^{*}\,F_1F_3 + 0.00808333^{*}\,F_1F_4 \\ &+ 4.58^{*}\,F_2F_3 + 16.4792^{*}\,F_2F_4 + 0.0544667^{*}\,F_3F_4 \\ &+ -0.00873531^{*}\,F_1\hat{}F_2 + -1235.31^{*}\,F_2\hat{}F_2 \\ &+ -0.0071746^{*}\,F_3\hat{}F_2 + -0.502125^{*}\,F_4\hat{}F_2\end{aligned}$$

The positive coefficient of F_1 (0.52302) suggests that a higher P4R concentration generally leads to higher removal efficiency.

The negative coefficient of F_2 in equation (−208.595) indicates that increasing the sorbent amount generally increases removal efficiency. The positive coefficient of F_3 (0.44245) implies that longer adsorption times generally result in higher removal efficiencies. Finally, the negative coefficient of F_4 (−0.301058) indicates that a lower pH (more acidic) generally leads to higher removal efficiencies.The equation also includes interaction terms (e.g., F_1F_2, F_2F_4) representing how the factors influence each other. These coefficients demonstrate that the relationship between the factors is not simply additive. For example, a positive coefficient for F_1F_2 suggests that the effect of increasing P4R concentration is more pronounced at higher sorbent amounts. Finally, the equation includes quadratic terms (e.g., $F_1\hat{}\,F_2$, $F_2\hat{}\,F_2$) representing the curvature of the relationship. Negative coefficients for these terms suggest that the effect of increasing each factor eventually diminishes, leading to a plateauing or even decreasing removal efficiency at higher values.

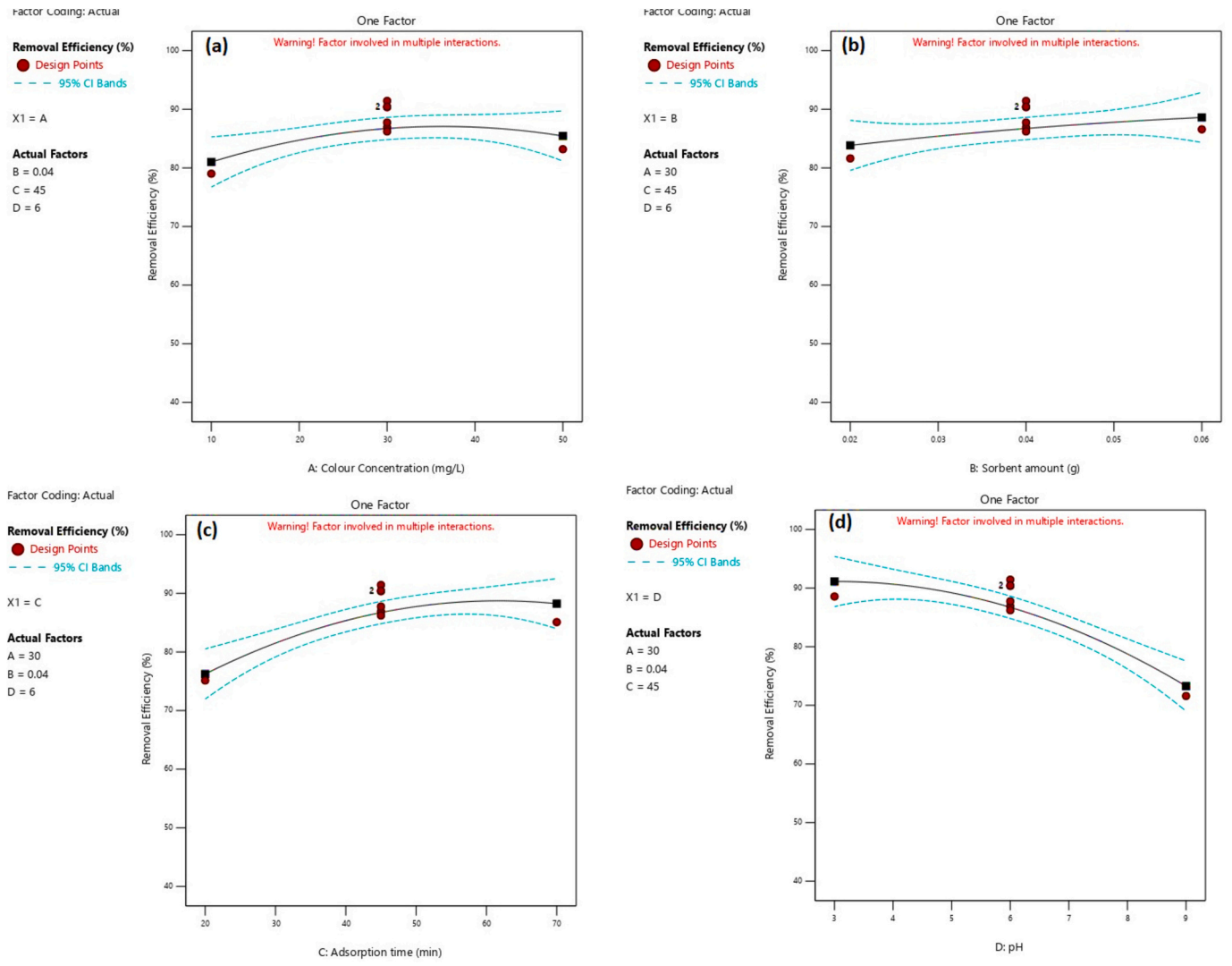

Fig. 3. Effects of each factor on the P4R removal.

3.6.1. *Numerical Optimization using LS Modelings*

In the standard probability plot models, there are more data points clustered around the central line, indicating that the distribution closely follows a normal pattern (**Fig. S1A**). The error plot of the residuals exhibited a random spread and a consistently even distribution of residuals across the predictions, showing no discernible pattern, which suggests that the proposed response surface models were effective in removing the P4R dye (**Fig. S1B**). **Fig. S1C** indicated a consistent agreement between the predicted and experimental results. Furthermore, the Box-Cox plot in **Fig. S1D** illustrated that the data adhered to a normal distribution, signifying the successful removal of the dye by the proposed model.

3.6.2. *Determining optimal points*

The optimal forecasted conditions for achieving maximum removal of P4R and the corresponding optimal removal efficiency are detailed in Table 2. Experimental results showed removal efficiency of 91.43 % was obtained by conducting experiments under the optimal parametric conditions using the LS model (pH 4.47, adsorbent dosage 0.047 g/L, contact time approximately 57.78 min, and initial P4R concentration 26.89 mg/L).

3.7. *ANN-RBF Modeling of Response Surface*

According to the results, the proposed ANN-RBF is 4–16-1, in which four input layers, one hidden layer with 16 neurons with Gaussian transfer functions, and one output layer (dye removal efficiency) were designed.

In the model, the correlation coefficient (R^2), P (LOF), and average error in training data were 0.98, 0.65, and 2.16, respectively. A high R^2 value of 0.98 indicates a strong correlation between the model's predictions and the actual P4R removal efficiency observed in the training data. This suggests that the model effectively captures the underlying relationships between the input factors and the output. P (LOF) likely refers to the *p*-value of the lack of fit for the presented method. A p-value of 0.65 indicates that the model is statistically significant and its predictive capabilities are not likely due to random chance. Besides, the low average error of 2.16 in the training data suggests that the model is accurate in its predictions with minimal deviations from the actual values. These results collectively indicate that the ANN-RBF model demonstrates a high level of accuracy and generalizability for predicting P4R removal efficiency.

Fig. S2A illustrates the relationship between the anticipated and nominal values for all sample analytes based on ANN modeling. The

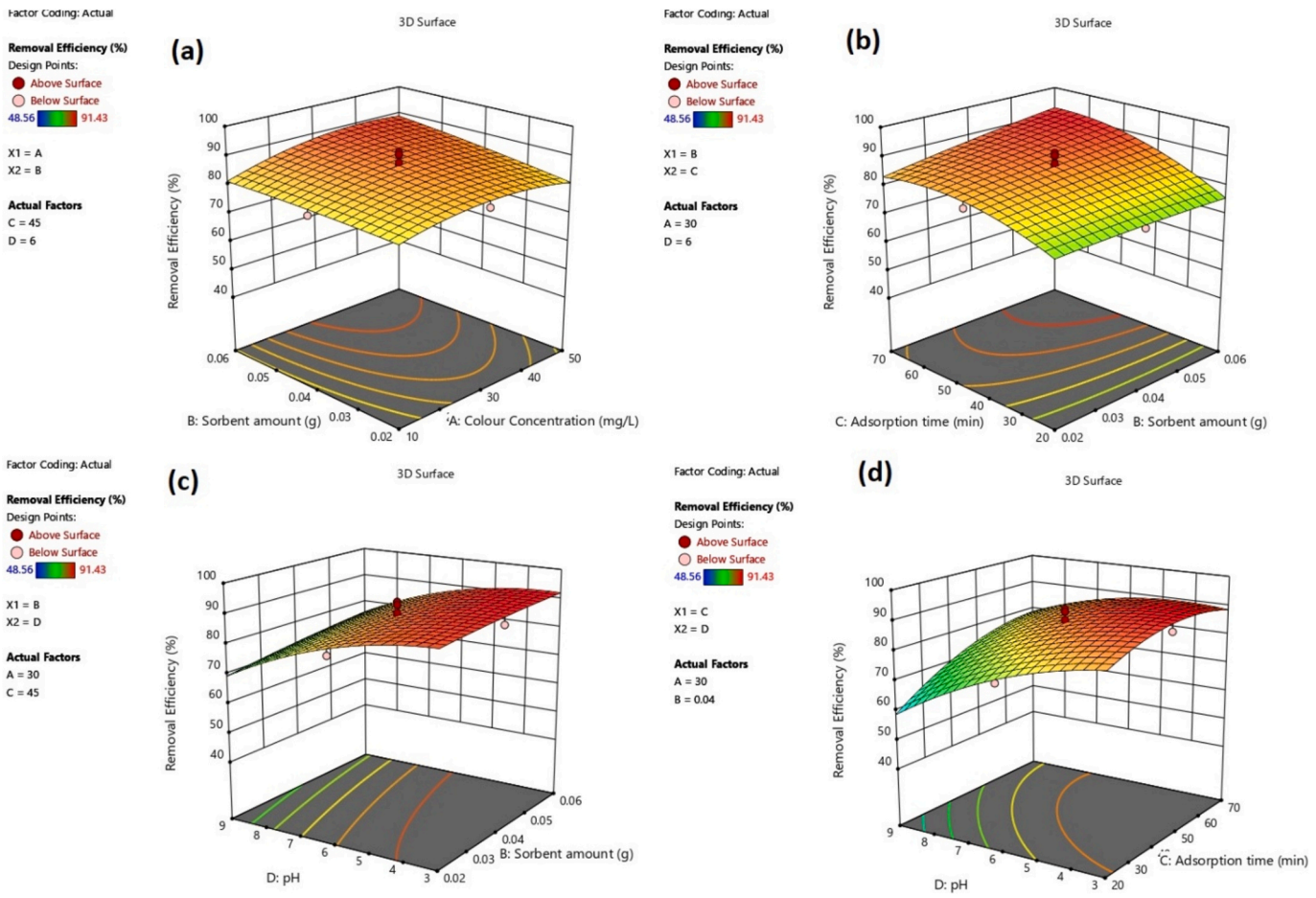

Fig. 4. Effects of the significant interactions on the P4R removal.

model exhibits favorable concordance with the empirical data. The error diagram of the residuals displayed a random scatter and a consistent range of residuals from top to bottom across the predictions, the non-observance of the obtained data from the specific pattern indicates the adequacy of the proposed response surface models for P4R color removal (**Fig. S2B).** Results demonstrates both RBF-ANN and LS models high predictive accuracy and superior model performance in predicting dye decolorization (%). The parametric method's potency was confirmed by comparing the design matrix and measured responses using a non-parametric approach using RBF-ANN.

Table 2 display both the experimental and predicted values (RBF-ANN and LS) for color removal efficiency (R_1) across 30 design runs. It is evident that most predicted values align closely with the experimental values. However, there are slight discrepancies between the ANN-RBF predicted values and the experimental values for color removal efficiency in Runs 9, 18, 22, 24, 27, and 28, indicating some variation in the results.

The LS predictions for color removal efficiency also differed from the experimental values in Runs 4, 7, 16, 17, and 30, with larger deviations observed in these cases. This could be due to outliers or data points that fall outside the predicted line, which can occur in any predictive model.

The research ultimately concluded that employing a complete quartic mathematical model is successful in establishing the relationship among substantial variables and investigational responses using central composite design.

3.8. Adsorption isotherm

An essential component in the design of adsorption systems is the equilibrium adsorption isotherm, as it establishes the connection between the amount of adsorbate and the equilibrium concentration in the solution. The research employed the two most widely utilized isotherms, Langmuir and Freundlich, from a range of available isotherm equations. The adsorption isotherm experiment was conducted at a pH of 4.47 for 57.78 min using a sorbent dosage of 0.047 g/L. The Eq demonstrating the Langmuir isotherm model is presented as Eq.(A.4) and Eq.(A.5) (Ghorbani et al., 2018, Heydari & Khavarpour, 2018):

$$\frac{C_e}{q_e} = \frac{C_e}{q_{max}} + \frac{1}{bq_{max}} \tag{A.4}$$

$$lnq_e = lnk_f + \frac{1}{n} lnC_e \tag{A.5}$$

Ce and qe represent the main dye concentration in the sample solution and the amount of adsorption at equilibrium per unit mass of sorbent (mg g^{-1}), respectively. Additionally, qmax, b, k_f, and n denote the maximum adsorption capacity of the monolayer (mg g^{-1}), the Langmuir constant (mg/L), the maximum adsorption capacity according to the Freundlich model (mg g^{-1}), and the adsorption intensity, respectively.

The parameters' values were determined, and the appropriate isotherm model was identified using the regression coefficient (R^2) through plotting Ce/qe versus Ce and ln qe versus ln Ce. The results indicate that the Freundlich isotherm **(Fig. S3B)** offers a more accurate prediction of dye adsorption by AmCs/$NiFe_2O_4$ NPs in comparison to the Langmuir isotherm (**Fig. S3A**). Consequently, it was deduced that the sorbent surface is heterogeneous, and adsorption predominantly occurs in multiple layers. These findings aligned with the observations derived from the SEM images of the sorbent. Adsorption intensity (n) is used to

Table 2
Comparison of experimental and predicted values for RSM and ANN-RBF models.

Run	A:Color Concentration (F_1)	B:Sorbent amount (F_2)	C:Adsorption time (F_3)	D:pH (F_4)	Removal Efficiency	Predicted Value LS	Predicted Value ANN-RBF
	mg/L	g	min		%	%	%
1	10	0.02	20	3	80.48	80.41	81.6457
2	10	0.04	45	6	79.01	81.01	81.3267
3	50	0.02	70	9	69.46	69.20	69.8256
4	30	0.06	45	6	86.58	88.61	87.7323
5	50	0.06	20	3	86.32	84.31	85.1192
6	50	0.02	20	9	55.08	55.84	55.9777
7	30	0.04	45	9	71.59	73.28	71.8572
8	50	0.02	20	3	81.74	82.86	81.3503
9	30	0.04	45	6	91.43	86.72	86.9829
10	30	0.04	20	6	75.13	76.24	74.6446
11	30	0.04	45	6	86.21	86.72	86.9829
12	10	0.06	70	9	78.53	77.34	78.7061
13	30	0.04	45	6	86.89	86.72	86.9829
14	10	0.02	70	3	81.46	81.88	81.0812
15	10	0.06	20	3	75.18	75.37	74.6008
16	50	0.06	70	3	88.14	90.49	89.272
17	30	0.02	45	6	81.62	83.84	82.4311
18	30	0.04	45	6	90.36	86.72	86.9829
19	30	0.04	45	6	87.75	86.72	86.9829
20	10	0.02	70	9	68.24	69.26	68.3688
21	10	0.06	70	3	87.76	86.00	85.7359
22	30	0.04	70	6	85.09	88.23	89.0964
23	50	0.02	70	3	82.68	79.88	80.6084
24	30	0.04	45	3	88.56	91.12	92.6175
25	10	0.02	20	9	53.86	51.45	52.0717
26	30	0.04	45	6	90.43	86.72	86.9829
27	50	0.04	45	6	83.19	85.44	86.6286
28	50	0.06	20	9	61.73	61.24	62.2749
29	50	0.06	70	9	84.68	83.76	82.5919
30	10	0.06	20	9	48.56	50.37	50.2328

Table 3
Adsorption kinetics and isotherms for P4R removal by AmCs/$NiFe_2O_4$ NPs.

Kinetic model	Equation	Parameters		R^2
Pseudo- first-order model	$log\,(q_e - q_t) = log\, q_e - \frac{k_1 t}{2.303}$	q_e (mg g^{-1}) K_1 (min^{-1})	146.72 0.068	0.9605
Pseudo- second-order model	$\frac{t}{q_t} = \frac{1}{k_2 q_e^2} + \frac{1}{q_e} t$	q_e (mg g^{-1}) K_2 (g mg^{-1} min^{-1})	125 0.000262	0.9916
Intra-particle diffusion model	$q_t = k_i * t^{\frac{1}{2}} + C$	K_i (mg g^{-1} $min^{-1/2}$)	10.89	0.9782

Isotherm model	Equation	Parameters		R^2
Langmuir model	$\frac{C_e}{q_e} = \frac{C_e}{q_{max}} + \frac{1}{b q_{max}}$	q_{max} (mg g^{-1}) b (L mg^{-1})	208.33 0.05	0.9682
Freundlich model	$lnq_e = lnk_f + \frac{1}{n} lnC_e$	K_f (mg g^{-1}) n	19.32 1.90	0.9888

evaluate the favorability of the adsorption procedure, with the ideal n falling between 1 and 10. The optimal n value is 1.90. The maximum adsorption capability (qmax) of P4R dye on AmCs/ $NiFe_2O_4$ NPs is 208.33 mg g^{-1} **(**Table 3**).**

3.9. Adsorption of kinetics

The adsorption kinetic data for P4R were analyzed using pseudo-first-order, pseudo-second-order, and intraparticle diffusion models.

The rate equation is defined as Eq.(A.6), Eq.(A.7) and Eq.(A.8), respectively (Moharram et al., 2016; Yousefi et al., 2019):

$$log(q_e - q_t) = log q_e - \frac{k_1 t}{2.303} \quad (A.6)$$

$$\frac{t}{q_t} = \frac{1}{k_2 q_e^2} + \frac{1}{q_e} t \quad (A.7)$$

$$q_t = k_i * t^{\frac{1}{2}} + C \quad (A.8)$$

Where qt and qe represent the quantity of dye adsorbed at equilibrium and at a specific time (mg g^{-1}), while k_1 and k_2 (g mg^{-1} min^{-1}) denote the rate constants for the adsorption process.

The study examined the influence of contact duration within the 10–80 min range under ideal conditions to assess the ability of kinetic models to predict the amount of dye adsorption by AmCs/ $NiFe_2O_4$ NPs (refer to Fig. 4S **and** Table 3).

The pseudo-first-order kinetic model explains a decelerating chemical adsorption process, where the number of unoccupied sites on the sorbent is proportional to the rate of adsorption.

Plotting log (qe-qt) against t yields a linear correlation, enabling the determination of k_1 and qe from the slope and y-intercept.

The experiments on the pseudo-first-order kinetic model (**Fig. S4A**) and intraparticle diffusion model (**Fig. S4C**) revealed significant nonlinearity and a decreased correlation coefficient. Reduced correlation coefficient values suggest limited dye diffusion within the sorbent pores, and the values of the intraparticle diffusion equation are distant from the origin, signifying its lack of significance in rate determination.

The graph for pseudo-second-order kinetics (**Fig. S4B**) shows a linear relationship between the t/qt values and t, caused in a great correlation coefficient. The second-order kinetic rate constant (k_2) and equilibrium adsorption capacity (qe) were calculated from the slope and y-intercept of the t/qt versus t graph, respectively.

The R^2 and qe values indicated that the pseudo-second-order kinetic model yielded superior outcomes. This suggests that the adsorption of P4R on AmCs/$NiFe_2O_4$ NPs is characterized as chemisorption. The

Table 4
Comparison of the various sorbents for P4R dye removal.

NO	Sorbent	Qe (mg g^{-1})	Time (min)	pH	sorbent dosage (g/L)	dye concentration (mg/L	Refs.
1	Alkali boiled Tilapia fish scales	134.40	240	7.6	0.24	10–50	(Zhu et al., 2013)
2	ZnAl-LDH/PVA	16.3	40	7	–	–	(Balayeva et al., 2023)
3	Fe_3O_4@SiO_2-CMK-8, MNCs)	78.74	20	2	0.1	50	(Toutounchi et al., 2021)
4	NH_2-MMNCs	58.8	30	2	0.08	50	(Sojoudi et al., 2016)
5	CTAB	15.470	15	4	6	–	(Kieu et al., 2024)
6	Activated carbon I	30.3	100	5	1.2	100	(Heibati et al., 2015)
7	chitosan/polyamide nanofibers	502.4	20	1	2	50	(Dotto et al., 2017)
8	AmCs/$NiFe_2O_4$	208.33	58.78	4.47	0.047	26.89	This work

removal efficiency exhibited an increase up to 57.78 min, after which it remained constant at higher durations, indicating a rapid adsorption process capable of reaching equilibrium in less than 80 min.

3.10. Real sample analysis

The dye P4R removal efficiency in the real sample (Pomegranate juices) was 90.34 %. The study found that P4R can be efficiently removed from fruit juice samples in a lab setting by using nanoparticles.

3.11. Recovery capability

From an economic perspective, the recoverability of the sorbent holds significance as it reflects the low cost of its use in elimination of contaminant, the stability of the adsorbed substantial on the surface of sorbent, and the regeneration ability of the sorbent. Following the elimination process, the sorbent underwent rinsing with deionized water and subsequent separation via a magnet. Next, a 0.2 M aqueous solution of ammonium (1.0 mL) was added to the sorbent and agitated for 15 min at 150 rpm. The sorbent was then rinsed with deionized water in preparation for reuse. The adsorption effectiveness of P4R dye by AmCs/$NiFe_2O_4$ NPs for up to 5 cycles exceeded 85 %, as depicted in (**Fig. S5A**). Any reduction in dye adsorption efficiency may be related to the following factors: insufficient dye separation, and sorbent, minor sorbent loss throughout the separation process, and structural degradation of the sorbent throughout the dye elimination phase. Subsequently, the developed nanocomposite serves as a durable and effective sorbent for P4R dye elimination, aligning via the documents of previous studies (Ansari et al., 2022) (Habiba et al., 2017).

The SEM image (**Fig. S5B**) indicates the presence of pores on the surface of AmCs/$NiFe_2O_4$ NPs, suggesting that a reduced number of pores can become saturated with the P4R dye throughout the adsorption procedure.

The sorbent XRD design the following five adsorption-desorption cycles is exposed in **Fig. S5C** to assess changes in the sorbent structure post-desorption. This pattern does not show any significant change in the structure of the absorber, only a slight decrease in the peak intensity compared to the original absorber pattern.

3.12. Comparison with other sorbents

The effectiveness of the created sorbent and other sorbents previously investigated for the elimination of P4R dye are equated in Table 4. The documents displays that the developed sorbent surpasses most prepared sorbents in terms of adsorption capacity. Sorbent No. 7 (chitosan/polyamide nanofibers) demonstrates a more absorption capability than the other sorbent. However, to achieve dye removal, more sorbent and a comparatively low acidic pH are required. It is noteworthy, however, that producing this sorbent involves many more steps and reagents than producing the sorbent used in the study. Consequently, the synthesized sorbent demonstrates the appropriate capacity for removing P4R dye from food samples, as well as the appropriate contact duration, adsorption capacity, and reusability, making it a strong contender for the job.

4. Conclusion

The result demonstrates the successful chitosan coating of $NiFe_2O_4$ NPs through XRD, FTIR, SEM, and TEM, revealing intricate electrostatic and chemical interactions and surface morphology transformation. This study achieved a maximum P4R removal of 91.43 % at a pH of 4.47, contact time of 57.78 min, AmCs/$NiFe_2O_4$ NPs dose of 0.047 g/L, and P4R concentration of 26.88 mg/L Furtheremore, this study compared the performance of an LS-based model and RBF-ANN in the removal of P4R dye from fruit juice samples. Both models provided good predictions for independent variables. The color elimination efficacy for real sample (Pomegranate juices) was approximately 90.34 %. The effectiveness, feasibility, and capability of this method were confirmed for commercial and traditional fruit juice samples. The importance of AmCs/$NiFe_2O_4$ NPs as a sorbent for removal of synthetic dyes lies in their high adsorption capacity, regeneration potential, environmental friendliness, and fast adsorption rate, making them a promising solution for addressing the challenges of synthetic dye removal in industrial settings.

CRediT authorship contribution statement

Samira Shokri: Writing – review & editing, Writing – original draft, Supervision, Methodology, Investigation. **Nabi Shariatifar:** Writing – review & editing, Writing – original draft, Supervision, Methodology, Investigation. **Ebrahim Molaee-Aghaee:** Writing – review & editing, Writing – original draft, Supervision, Investigation. **Gholamreza Jahed Khaniki:** Writing – review & editing, Writing – original draft, Methodology, Investigation. **Parisa Sadighara:** Writing – review & editing, Writing – original draft, Methodology, Investigation. **Somaye Vali Zade:** Writing – review & editing, Writing – original draft, Methodology, Investigation. **Shahram Shoeibi:** Writing – review & editing, Writing – original draft, Investigation.

Declaration of competing interest

The authors state that they do not have any known conflicting financial interests or personal relationships that could impact the findings presented in this manuscript.

Data availability

The data that has been used is confidential.

Acknowledgment

This work is based upon research funded by Iran National Science Foundation (INSF) under project No.4025197.

Appendix A. Supplementary data

Supplementary data to this article can be found online at https://doi.org/10.1016/j.fochx.2024.101856.

References

Ackah, M., Anim, A. K., Zakaria, N., Osei, J., Saah-Nyarko, E., Gyamfi, E. T., … Bentil, N. O. (2014). Determination of some heavy metal levels in soft drinks on the Ghanaian market using atomic absorption spectrometry method. *Environmental Monitoring and Assessment, 186*, 8499–8507.

Ahmad, M. F., Hassan, S., Imran, Z., Mazhar, D., Afzal, S., & Ullah, S. A. (2023). Green approach to water purification: Investigating methyl Orange dye adsorption using chitosan/polyethylene glycol composite membrane. *Journal of Polymers and the Environment*, 1–19.

Ahmad, T., Bae, H., Iqbal, Y., Rhee, I., Hong, S., Chang, Y., … Sohn, D. (2015). Chitosan-coated nickel-ferrite nanoparticles as contrast agents in magnetic resonance imaging. *Journal of Magnetism and Magnetic Materials, 381*, 151–157.

Ansari, M. J., Jasim, S. A., Bokov, D. O., Thangavelu, L., Yasin, G., & Khalaji, A. D. (2022). Preparation of new bio-based chitosan/Fe2O3/NiFe2O4 as an efficient removal of methyl green from aqueous solution. *International Journal of Biological Macromolecules, 198*, 128–134.

Balayeva, O. O., Azizov, A. A., Muradov, M. B., & Alosmanov, R. M. (2023). Removal of tartrazine, ponceau 4R and patent blue V hazardous food dyes from aqueous solutions with ZnAl-LDH/PVA nanocomposite. *Journal of Dispersion Science and Technology, 44*, 1133–1146.

Carabajal, M., Teglia, C. M., Cerutti, S., Culzoni, M. J., & Goicoechea, H. C. (2020). Applications of liquid-phase microextraction procedures to complex samples assisted by response surface methodology for optimization. *Microchemical Journal, 152*, Article 104436.

Choi, H. (2012). Risk assessment of daily intakes of artificial colour additives in food commonly consumed in Korea. *Journal of Food and Nutrition Research, 51*, 13–22.

Çınar, S., Kaynar, Ü. H., Aydemir, T., Kaynar, S.Ç., & Ayvacıklı, M. (2017). An efficient removal of RB5 from aqueous solution by adsorption onto nano-ZnO/chitosan composite beads. *International Journal of Biological Macromolecules, 96*, 459–465.

Dehelean, A. (2013). Magdas DA (2013): Analysis of mineral and heavy metal content of some commercial fruit juices by inductively coupled plasma mass spectrometry. *The Scientific World Journal, 1*, 215423.

Dotto, G., Santos, J., Tanabe, E., Bertuol, D., Foletto, E., Lima, E., & Pavan, F. (2017). Chitosan/polyamide nanofibers prepared by Forcespinning® technology: A new adsorbent to remove anionic dyes from aqueous solutions. *Journal of Cleaner Production, 144*, 120–129.

Ghorbani, M., Ariavand, S., Aghamohammadhasan, M., & Seyedin, O. (2021). Synthesis and optimization of a green and efficient sorbent for removal of three heavy metal ions from wastewater samples: Kinetic, thermodynamic, and isotherm studies. *Journal of the Iranian Chemical Society, 18*, 1947–1963.

Ghorbani, M., Shams, A., Seyedin, O., & Afshar Lahoori, N. (2018). Magnetic ethylene diamine-functionalized graphene oxide as novel sorbent for removal of lead and cadmium ions from wastewater samples. *Environmental Science and Pollution Research, 25*, 5655–5667.

Giordano, P. C., Goicoechea, H. C., & Olivieri, A. C. (2017). SRO_ANN: An integrated MatLab toolbox for multiple surface response optimization using radial basis functions. *Chemometrics and Intelligent Laboratory Systems, 171*, 198–206.

Gordi, Z., Ghorbani, M., & Ahmadian Khakhiyani, M. (2020). Adsorptive removal of enrofloxacin with magnetic functionalized graphene oxide@ metal-organic frameworks employing D-optimal mixture design. *Water Environment Research, 92*, 1935–1947.

Habiba, U., Afifi, A. M., Salleh, A., & Ang, B. C. (2017). Chitosan/(polyvinyl alcohol)/zeolite electrospun composite nanofibrous membrane for adsorption of Cr6+, Fe3+ and Ni2+. *Journal of Hazardous Materials, 322*, 182–194.

Heibati, B., Rodriguez-Couto, S., Al-Ghouti, M. A., Asif, M., Tyagi, I., Agarwal, S., & Gupta, V. K. (2015). Kinetics and thermodynamics of enhanced adsorption of the dye AR 18 using activated carbons prepared from walnut and poplar woods. *Journal of Molecular Liquids, 208*, 99–105.

Helal, E. G., El-Kassas, M. A., Zaahkouk, S. A., Abdel-Wahed, H. G., & Mahmoud, A. F. (2006). Some biochemical parameters of young male albino rats treated with ponceau 4 R and vitamin E. *The Egyptian Journal of Hospital Medicine, 22*, 73–79.

Heydari, R., & Khavarpour, M. (2018). Adsorption of malachite green from aqueous solution by nanozeolite clinoptilolite: Equilibrium, kinetic and thermodynamic studies. *International Journal of Engineering, 31*, 1–11.

Homayonfard, A., Miralinaghi, M., Mohammad, H. S., Shirazi, R., & Moniri, E. (2020). Removal of cd (II) ion from aqueous solution using nickel ferrite magnetic nanoparticles cross–linked chitosan. *Journal of Water and Wastewater; Ab va Fazilab (in persian), 31*, 112–127.

Hong, E., Lee, S. Y., Jeong, J. Y., Park, J. M., Kim, B. H., Kwon, K., & Chun, H. S. (2017). Modern analytical methods for the detection of food fraud and adulteration by food category. *Journal of the Science of Food and Agriculture, 97*, 3877–3896.

Kefeni, K. K., Mamba, B. B., & Msagati, T. A. (2017). Application of spinel ferrite nanoparticles in water and wastewater treatment: A review. *Separation and Purification Technology, 188*, 399–422.

Kieu, T. T., Nguyen, T. T. T., Truong, T. T. T., Hoang, D. T., Vu, T. L. C., Nguyen, T. M. T., … Pham, T. D. (2024). Surface modification of zeolite by cationic surfactant and the application on adsorptive removal of azo dye Ponceau 4R. *Journal of Molecular Structure, 1304*, Article 137619.

Masood, M. H., Haleem, N., Shakeel, I., & Jamal, Y. (2020). Carbon dioxide conversion into the reaction intermediate sodium formate for the synthesis of formic acid. *Research on Chemical Intermediates, 46*, 5165–5180.

Moharram, M. A. K., Tohami, K., El Hotaby, W. M., & Bakr, A. M. (2016). Graphene oxide porous crosslinked cellulose nanocomposite microspheres for lead removal: Kinetic study. *Reactive and Functional Polymers, 101*, 9–19.

Mustafa, I. (2019). Methylene blue removal from water using H2SO4 crosslinked magnetic chitosan nanocomposite beads. *Microchemical Journal, 144*, 397–402.

Oliveri, P., & Downey, G. (2012). Multivariate class modeling for the verification of food-authenticity claims. *TrAC Trends in Analytical Chemistry, 35*, 74–86.

Pervukhin, D., Davardoost, H., Kotov, D., Ilyukhina, Y., & Hasanov, K. (2023). *A SUSTAINABLE DEVELOPMENT GOALS-BASED MATHEMATICAL MODEL FOR SELECTING OIL AND GAS INVESTMENT PROJECTS UNDER UNCERTAINTY AND LIMITED RESOURCES. Advanced Mathematical Models & Applications 8*.

Piccin, J. S., Vieira, M., Gonçalves, J., Dotto, G., & Pinto, L. A. A. (2009). Adsorption of FD&C red no. 40 by chitosan: Isotherms analysis. *Journal of Food Engineering, 95*, 16–20.

Ramezani, S., Ghazitabar, A., & Sadrnezhaad, S. K. (2016). Synthesis and characterization of chitosan coating of NiFe 2 O 4 nanoparticles for biomedical applications. *Journal of the Iranian Chemical Society, 13*, 2069–2076.

Reddy, D. H. K., & Lee, S.-M. (2013). Application of magnetic chitosan composites for the removal of toxic metal and dyes from aqueous solutions. *Advances in Colloid and Interface Science, 201*, 68–93.

Rezagholizade-shirvan, A., Masrournia, M., Fathi Najafi, M., & Behmadi, H. (2023). Synthesis and characterization of nanoparticles based on chitosan-biopolymers systems as nanocarrier agents for curcumin: Study on pharmaceutical and environmental applications. *Polymer Bulletin, 80*, 1495–1517.

Rezagholizade-shirvan, A., Najafi, M. F., Behmadi, H., & Masrournia, M. (2022). Preparation of nano-composites based on curcumin/chitosan-PVA-alginate to improve stability, antioxidant, antibacterial and anticancer activity of curcumin. *Inorganic Chemistry Communications, 145*, Article 110022.

Roosta, M., Ghaedi, M., Sahraei, R., & Purkait, M. (2015). Ultrasonic assisted removal of sunset yellow from aqueous solution by zinc hydroxide nanoparticle loaded activated carbon: Optimized experimental design. *Materials Science and Engineering: C, 52*, 82–89.

Rose, P. K., Kumar, R., Kumar, R., Kumar, M., & Sharma, P. (2023). Congo red dye adsorption onto cationic amino-modified walnut shell: Characterization, RSM optimization, isotherms, kinetics, and mechanism studies. *Groundwater for Sustainable Development, 21*, Article 100931.

Rouhani, S., & Pirkarimi, A. (2018). A review on analytical procedures azo dyes in the food industry. *Journal of Studies in Color World, 7*, 19–36.

Sadegh, N., Haddadi, H., & Asfaram, A. (2022). Synthesis of a green magnetic biopolymer derived from oak fruit hull tannin for the efficient and simultaneous adsorption of a mixture of malachite green and sunset yellow dyes from aqueous solutions. *New Journal of Chemistry, 46*, 11862–11876.

Shokri, S., Shariatifar, N., Molaee-Aghaee, E., Jahed Khaniki, G., Sadighara, P., & Faramarzi, M. A. (2024). Modeling sunset yellow removal from fruit juice samples by a novel chitosan-nickel ferrite nano sorbent. *Scientific Reports, 14*, 208.

Shokri, S., Shariatifar, N., Molaee-Aghaee, E., Khaniki, G. J., Sadighara, P., Faramarzi, M. A., … Rezagholizade-Shirvan, A. (2023). Synthesis and characterization of a novel magnetic chitosan–nickel ferrite nanocomposite for antibacterial and antioxidant properties. *Scientific Reports, 13*, 15777.

Sojoudi, M., Shariati, S., & Khabazipour, M. (2016). Amine functionalized Kit-6 mesoporous magnetite nanocomposite as an efficient adsorbent for removal of Ponceau 4R dye from aqueous solutions. *Analytical and Bioanalytical Chemistry Research, 3*, 287–298.

Solano, R. A., De León, L. D., De Ávila, G., & Herrera, A. P. (2021). Polycyclic aromatic hydrocarbons (PAHs) adsorption from aqueous solution using chitosan beads modified with thiourea, TiO2 and Fe3O4 nanoparticles. *Environmental Technology & Innovation, 21*, Article 101378.

Stozhko, N. Y., Khamzina, E. I., Bukharinova, M. A., & Tarasov, A. V. (2022). An electrochemical sensor based on carbon paper modified with graphite powder for sensitive determination of sunset yellow and tartrazine in drinks. *Sensors, 22*, 4092.

Teglia, C. M., Guiñez, M., Goicoechea, H. C., Culzoni, M. J., & Cerutti, S. (2020). Enhancement of multianalyte mass spectrometry detection through response surface optimization by least squares and artificial neural network modelling. *Journal of Chromatography A, 1611*, Article 460613.

Toutounchi, S., Shariati, S., & Mahanpoor, K. (2021). Application of magnetic ordered mesoporous carbon nanocomposite for the removal of Ponceau 4R using factorial experimental design. *Silicon, 13*, 1561–1573.

Tsai, F.-C., Ma, N., Chiang, T.-C., Tsai, L.-C., Shi, J.-J., Xia, Y., … Chuang, F.-S. (2014). Adsorptive removal of methyl orange from aqueous solution with crosslinking chitosan microspheres. *Journal of Water Process Engineering, 1*, 2–7.

Tsuda, S., Murakami, M., Matsusaka, N., Kano, K., Taniguchi, K., & Sasaki, Y. F. (2001). DNA damage induced by red food dyes orally administered to pregnant and male mice. *Toxicological Sciences, 61*, 92–99.

Wan, S., Wu, J., Zhou, S., Wang, R., Gao, B., & He, F. (2018). Enhanced lead and cadmium removal using biochar-supported hydrated manganese oxide (HMO) nanoparticles: Behavior and mechanism. *Science of the Total Environment, 616*, 1298–1306.

Yoshioka, N., & Ichihashi, K. (2008). Determination of 40 synthetic food colors in drinks and candies by high-performance liquid chromatography using a short column with photodiode array detection. *Talanta, 74*, 1408–1413.

Yousefi, M., Farzadkia, M., Mahvi, A. H., Kermani, M., Gholami, M., & Esrafili, A. (2024). Photocatalytic degradation of ciprofloxacin using a novel carbohydrate-based nanocomposite from aqueous solutions. *Chemosphere, 349*, Article 140972.

Yousefi, M., Nabizadeh, R., Alimohammadi, M., Mohammadi, A. A., & Mahvi, A. H. (2019). Removal of phosphate from aqueous solutions using granular ferric hydroxide process optimization by response surface methodology. *Desalination and Water Treatment, 158*, 290–300.

Yuvaraja, G., Chen, D.-Y., Pathak, J. L., Long, J., Subbaiah, M. V., Wen, J.-C., & Pan, C.-L. (2020). Preparation of novel aminated chitosan schiff's base derivative for the removal of methyl orange dye from aqueous environment and its biological applications. *International Journal of Biological Macromolecules, 146*, 1100–1110.

Zhu, K., Gong, X., He, D., Li, B., Ji, D., Li, P., … Luo, Y. (2013). Adsorption of Ponceau 4R from aqueous solutions using alkali boiled Tilapia fish scales. *RSC Advances, 3*, 25221–25230.